Biospherical Instruments Inc.

Biospherical Shadowband Accessory for Diffuse Irradiance (BioSHADE): A Marine Shadowband and GPS Accessory

Germar Bernhard, Charles R. Booth, John H. Morrow,

and Stanford B. Hooker

When citing this work, please use the following:

Bernhard, G., C.R. Booth, J.H. Morrow, and S.B. Hooker, 2010: "Biospherical Shadowband Accessory for Diffuse Irradiance (BioSHADE): A Marine Shadowband and GPS Accessory." In: J.H. Morrow, S.B. Hooker, C.R. Booth, G. Bernhard, R.N. Lind, and J.W. Brown, Advances in Measuring the Apparent Optical Properties (AOPs) of Optically Complex Waters, *NASA Tech. Memo. 2010–215856,* NASA Goddard Space Flight Center, Greenbelt, Maryland, 51–59.

5340 Riley Street
San Diego, CA 92110-2621 USA

Vox: +1.619.686.1888
Fax: +1.619.686.1887

Net: sales@biospherical.com
Web: www.biospherical.com

Chapter 5

Biospherical Shadowband Accessory for Diffuse Irradiance (BioSHADE): A Marine Shadowband and GPS Accessory

Germar Bernhard, Charles R. Booth, and John H. Morrow
Biospherical Instruments Inc.
San Diego, California

Stanford B. Hooker
NASA Goddard Space Flight Center
Greenbelt, Maryland

Abstract

BioSHADE is an accessory for shipboard radiometers that is used to measure the optical properties of the atmosphere while providing the usual global irradiance measurement of a solar reference. It meets the need for improving the self-shading correction applied to in-water AOP measurements, wherein atmospheric complexity makes it more difficult to properly model the diffuse irradiance. It also provides for the capability of several atmospheric data products that are useful to the atmospheric correction part of calibration and validation activities. BioSHADE integrates seamlessly into instrument systems based on the microradiometer architecture, although it can be configured for use with the PRR-800 series of solar references or other irradiance sensors with the same form factor. It is composed of the following components: a) the stepping motor and controller unit housing an Mdrive 17 from IMS Systems, b) a data aggregator derived from the microradiometer product line, c) a power regulation subsystem, d) the housing for the electromechanical components, e) the shadowband subassembly, and f) the radiometer mounting components. The BioGPS is a 12-satellite GPS receiver designed to be operated simultaneously with radiometric instruments. The system can be fully integrated with instrumentation based on the microradiometer architecture, wherein the GPS is operated over a single cable, linking radiometers, and the BioSHADE accessory with the BioGPS. The latter ensures the accessory components and the radiometric sensors can be operated using standard cabling and deck box configurations.

5.1 Introduction

BioSHADE is an accessory for shipboard radiometers that attaches to a solar reference. It is used to measure the optical properties of the atmosphere as part of a separate data acquisition sequence. BioSHADE meets the need for improving the self-shading correction applied in coastal waters wherein atmospheric complexity makes it more difficult to properly model the diffuse irradiance. It was designed to be used during the time period when a free-fall profiler is being hauled up to the surface. This normally takes only a few minutes (depending on water depth and environmental conditions), so the design parameters established for making the shadowband measurement were based on a 90 s acquisition event. When not being used, the solar reference is able to make an uncontaminated global irradiance measurement.

A GPS can provide vital cruise track and time-of-event records for post-processing optical data collected aboard ship. The U.S. GPS consists of a constellation of medium Earth-orbit satellites operated by the Department of Defense, but having public access. Each satellite in the constellation continually transmits a microwave stream containing time and position information. After locking onto multiple satellites, a GPS receiver converts small differences in the arrival times of these transmissions into a calculated position on the ground. The accuracy and precision of the resulting geographic coordinates usually satisfies most oceanographic sampling requirements.

BioGPS is a 12-satellite GPS receiver designed to be operated simultaneously with BSI radiometric instruments. The system can be fully integrated with optical instruments based on the MMS architecture, wherein the GPS is operated over a single cable linking radiometers and the BioSHADE accessory with the BioGPS. When PRR systems, such as BioSORS, are deployed, BioGPS is used in a stand-alone configuration, remotely delivering data to a logging computer via an independent cable.

5.2 Description

BioSHADE is composed of several components: a) the stepping motor and controller unit housing an Mdrive 17 from IMS Systems, b) a data aggregator derived from the BSI microradiometer product line, c) a power regulation subsystem, d) the housing for the electromechanical components, e) the shadowband subassembly, and f) the radiometer mounting components. The motor is controlled by an aggregator, which is a microprocessor-controlled module also derived from the BSI microradiometer product line. The aggregator allows seamless integration of the BioSHADE accessory into a network of sensors built with this technology. The power regulation subsystem provides the needed optimum power to the motor (12.2 V) and the aggregator (6.4 V), as well as power (6.4 V) to other microradiometer and BioGPS systems. The mounting system is currently based on 1 in national pipe tapered (NPT) type 316 stainless steel (SS) pipe and fittings, although alternative mounting configurations are possible.

The BioGPS combines a high sensitivity GPS microcontroller with a microradiometer aggregator module. The aggregator allows the data stream from the GPS module to be integrated into any system conforming to the MMS architecture, e.g., from a multichannel solar irradiance sensor. The aggregator has two communications ports, one for upstream communications to the deck box and subsequently, the data acquisition computer, and the other for downstream communications.

5.3 Design

The design of the BioSHADE accessory is optimized for 19-channel microradiometer solar references operated in a shipboard environment. The use of a shadowband on a ship requires a different optical design than for terrestrial shadowband photometers. Most notably, it is not possible to position a partial shadowband in accordance with a fixed geographic location, because the heading of the ship is usually not constant, nor is the vertical orientation (pitch and roll) of the device. The dimensions and geometry of the shadowband assembly, therefore, are constrained by the following requirements:

- When the centers of the Sun, shadowband, and diffuser align, the cosine collector must be completely shaded from all parts of the solar disk.
- Because the shadowband is moving at a constant speed, the size of the shadow should be sufficiently large such that the diffuser is shaded for at least seven sample points. (It was determined that this number of sample points is sufficient to ascertain unambiguously that the shading of the Sun is complete.)
- The width of the shadowband should be as small as possible to minimize the area of the sky that is shaded. This requirement helps reduce the uncertainties involved in calculating the direct irradiance component of the global irradiance.
- For practical reasons, the diameter of the shadowband should not be larger than 10 in (25 cm).
- A 180° swath of the shadowband should be completed in approximately 60 s (3° s^{-1} rotation rate), which when coupled with the rest of the command set, should result in a total data acquisition scenario of about 90 s.
- The shadowband should be out of the FOV of the cosine collector when moved to its lowest position for accurately measuring the global irradiance.

Using these requirements, the nominal inside diameter of the band is 8.56 in.

The band is made out of 0.06 in (1.5 mm) thick aluminum that is 1.0 in (2.5 cm) wide and anodized black. The size of the main housing is 3.5 in (8.9 cm) in diameter and 10.5 in (26.7 cm) long. A depiction of the BioSHADE accessory in operation with a microradiometer solar reference and BioGPS unit is shown in Fig. 50.

Fig. 50. A shadowband assembly schematic with a 19-channel microradiometer solar reference in the left foreground, the motor housing with supporting electronics at the right, and an optional BioGPS unit at the left rear. The narrow cylinder at center is the mounting post (1 in NPT 316SS pipe).

The minimum width of the shadowband is constrained by the size of the cosine collector, which is 0.885 in (2.25 cm) in diameter for BioSORS and C-OPS. Because the angular size of the solar disk is about 0.54°, the shadowband must be slightly wider. The requirement that the diffuser

should be shaded for at least seven sample points further increases the width.

Based on these considerations, the following dimensions were chosen: the shadowband is 1.00 in (2.54 cm) wide. The distance from the collector to the band depends on the orientation of the band. It varies from 3.78 in (9.60 cm) to 4.28 in (10.87 cm), because the pivot point is 0.5 in (1.27 cm) below the plane of the irradiance collector (also referred to as the *horizon*) to satisfy the last requirement above. When the band is in the zenith, it shades a 15°-wide segment of the sky. In the normal mode, the radiometer is sampling at a rate of 15 Hz. The measurement of seven sample points, therefore, requires 0.47 s during which the shadowband moves 1.2°.

The BioSHADE motor is a size 17 stepper motor with 51,200-step resolution, which is coupled to the shadowband with a flexible coupling (Fig. 51). The system has an expected range of motion of approximately 220°. The motor is equipped with a home sensor used in initial setup. Motor power is switched and provisions are made to measure internal voltage and current to allow automatic compensation for variable cable lengths and the resulting uncertainty of voltage drops. The supply voltage ranges from 12.75–16.00 VDC depending on the configuration and length of the cable. The system consumes up to 440 mA when fully configured with the actual voltage required. Most cases can be handled with a specification of 1 A.

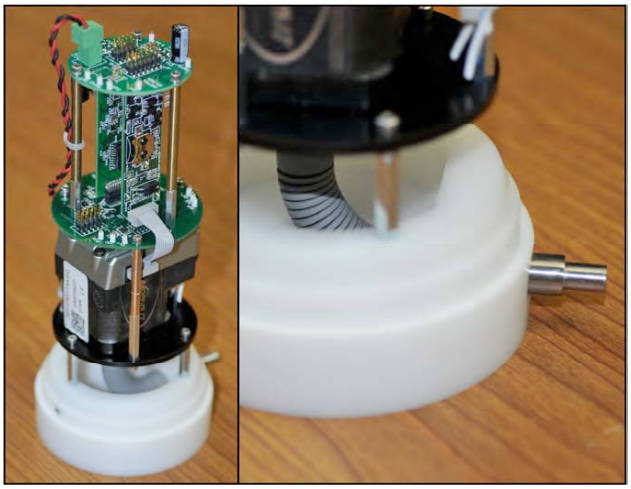

Fig. 51. The BioSHADE drive components (left), with the stepper motor above the white end cap; above the motor is the aggregator (vertically oriented green circuit board), which serves as the motor controller and electronic interface. A magnified view (right) shows the coupler in more detail. The unit is upside down in both panels.

To keep the shadowband at or below the horizon when stowed, the band needs space to rotate below the plane of the cosine collector. For the stowed angle below the horizon to be reasonably large (e.g., 40°), the clearance of the band with respect to the solar reference must be reasonably large. The needed clearance produces an eccentricity in the geometry of the band with respect to the sensor, which is shown in Fig. 52. Not shown in the figure, but used in the formulation of data products produced from the shadowband measurements, is the shadowband angle, v, which is defined as the angle between the horizontal plane of rotation and the direction of the shadowband (measured from the zero position, which is described below).

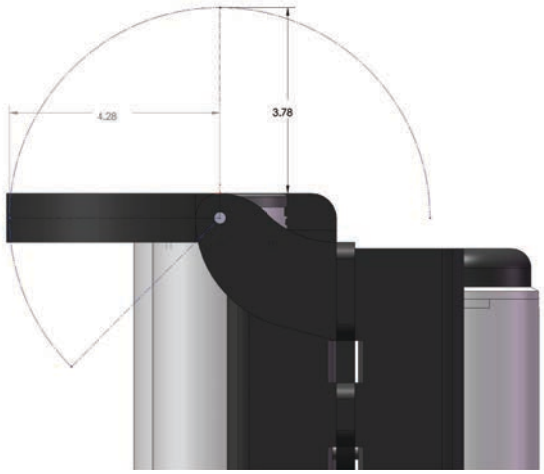

Fig. 52. A side-view illustration of the C-OPS solar reference with the BioSHADE, showing the distance between the shadowband and the diffuser for vertical and horizontal orientation of the shadowband. The BioSHADE housing is behind the solar reference (left) and the BioGPS is to the right.

5.4 GPS Operation

BioGPS can be used by itself or as part of more complicated systems, which need not be MMS instruments, although cabling and data acquisition is simplified when it is used as part of a microradiometer system. Five different modes of operation are available:

1. Fully integrated microradiometer system with a synchronized shadowband and GPS data stream controlled MMS deck box;
2. Automated shadowband movement and GPS reporting controlled by an MMS deck box;
3. Manual shadowband movement and GPS reporting controlled by a data acquisition computer;
4. Streaming GPS reporting using ASCII data; and
5. Polled GPS reporting using ASCII data.

The GPS data stream provides the following parameters: a) Universal Time Coordinated (UTC) to the nearest second, b) longitude, c) latitude, and d) the number of satellites visible. In the event that a GPS fix is invalid, `-999` is reported for each parameter.

Because the MMS architecture requires synchronized data streams at rates exceeding 12 Hz, the response times

of individual sensors are critical. In contrast, the GPS engine used in BioGPS typically updates its position once per second. This slow refresh rate has implications in the way the data is buffered by the BioGPS aggregator.

The BioGPS aggregator controls the sampling of the GPS, and also responds to polled requests for data from the controlling deck box. The service time of the requests is typically less than 10 ms to maintain a 15 Hz polled data stream from multiple radiometers, and other devices such as a shadowband. This need for very short lag times means that querying the GPS and then waiting for a response would greatly slow down the system. Consequently, the GPS data stream is serviced by interrupts, because the desired sample rate (nominally 15 Hz or 67 ms per frame) is too short to request and receive data in many instances. The best-case turnaround time period is approximately 35 ms, with many lasting 100 ms or longer, which is too long to wait for a reply without disturbing the sample rate.

The data volume of MMSs can be substantial. For example, three 19-channel radiometers are projected to have 332 bytes transmitted in each data frame (104 bytes per sensor plus about 20 bytes from the deck box). At 15 Hz, this is 4,980 bytes per second, or for a system running continuously, 480 MB per day. Although many radiometric systems have intermittent duty cycles (e.g., C-OPS), others will have more frequent sampling scenarios (e.g., OSPREy), so data volume can be an important problem.

The GPS data stream conforms to the National Marine Electronics Association (NMEA) data format, which is an ASCII string of up to 80 characters. The BioGPS command structure allows the full ASCII data stream to be retrieved. To minimize the flow of redundant data, however, the NMEA string can optionally be converted to short precision (4-byte) floating point numbers. Because fresh GPS data is only available every second, the data stream can be multiplexed, with the parameter actually transmitted being rotated through the four types of parameters (time, longitude, latitude, and number of satellites). This feature further reduces the amount of data to be transmitted.

5.5 Shadowband Operation

The precise position of the shadowband is unknown when the controller unit is powered up. When under the automatic control with a C-OPS deck box, the motor is turned on and initialized at startup. First, the motor is moved counterclockwise (CCW) approximately 20°, then back and forth 15° while deck box power levels are adjusted to compensate for any voltage drop in long cables.

The second part of the initialization sequence, which is issued by the data acquisition software, involves the following command sequences:

1. `Read` the motor position.
2. `Move` negative 12,000 steps from the current read position. This move ensures that the shadowband will find the home position in Step 3, regardless of its initial position. On some occasions, the shadowband may run into stops that are integral to the device's mounting brackets, causing the motor to slip (which is acceptable).
3. `Move` into the home position (this is always in the clockwise, CW, direction).
4. `Move` to the 0 (zero) position in the negative direction (CCW), approximately 30,000 steps. The exact value is the motor *offset* and will vary from unit to unit depending on the location of the home position.
5. `Set` this position to 0. This should have the band horizontal and even with the top of the irradiance collector.
6. `Move` the shadowband from 0–180° (which is the aforementioned v angle), with farther extension to a typical value of 220°, where the band is completely below the horizon. This latter position is also the *stowed* position when not in use.
7. `Move` the shadowband back to 0°; repeat Steps 6 and 7 as long as desired.

Extension of the motion cycle as part of the sixth step also provides an extended period of time with the band out of the field of view of the collector, so the data acquisition sequence ends with a global irradiance measurement. If the shadowband data is collected immediately after a C-OPS down cast, the global irradiances from the two events can be used to verify atmospheric stability across the measurement sequences. A sequential movement of the shadowband over the C-OPS solar reference during clear-sky conditions is shown in Fig. 53.

5.6 Shadowband Modeling and Testing

In the following discussion, BioSHADE was operated with a 19-channel C-OPS solar reference radiometer on the roof calibration facility at BSI. Weather conditions were ideal during the test period, offering several cloudless days with low aerosol loading. This analysis focuses on measurements taken on 7 October 2008, one of the clearest days of the test period.

Figure 54 shows solar reference measurements during a full cycle of shadowband irradiance at 320 nm (blue data set, right axis) and 780 nm (red data set, left axis) measured on 7 October 2008 between 17:52 and 17:56 UT. During this period, the solar zenith angle (SZA) was about 45.5°. Vertical lines indicate times when the motion of the shadowband reversed. The band is in its maximum position at points G_1 and G_3, and in the zero position at point G_2. As the band moves upward from point G_1, it will eventually be horizontal (point A_1). From this position onward, a portion of the sky will be shaded and the irradiance measured by the microradiometer will decrease. The change in signal is much larger at 320 nm than 780 nm, because sky radiance is much greater at shorter wavelengths (at 780 nm, the predominant portion of the signal is due to direct sunlight).

Fig. 53. A sequential movement of the shadowband over the C-OPS solar reference (center white cylinder) on a clear-sky day. The shadowband controller is the right-most cylinder, and the GPS is the left-most. The solar reference is slightly above the other two devices to ensure an unobstructed view of the sky. The primary cable connection is to the controller; the other devices plug into the controller to receive power and send data. The black cylinder between the BioGPS and the solar reference is a solar reference for another instrument system.

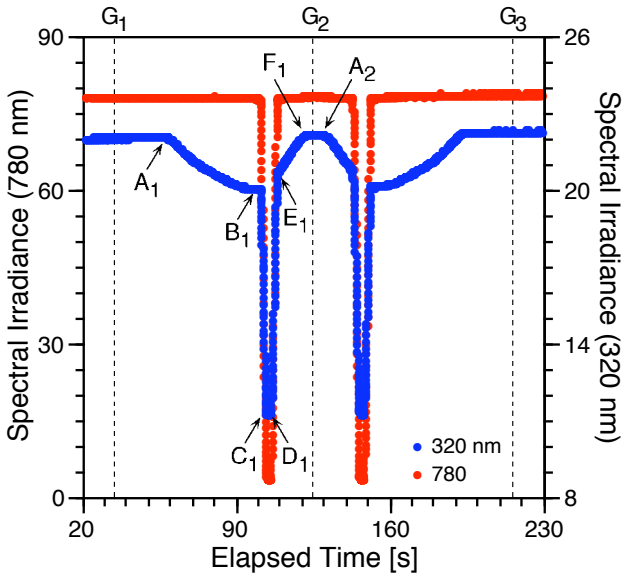

Fig. 54. The spectral irradiance measurement at 320 and 780 nm using the prototype BioSHADE accessory and the C-OPS solar reference. The data were acquired on 7 October 2008 between 1752 and 1756 UTC. Vertical lines indicate times when the motion of the shadowband reversed. Labeled points are explained in the text.

The collector of the solar reference is cosine weighted and the effect of shading the sky increases as the band moves from the horizon toward the zenith. At point B_1 in Fig. 54, the band starts to block the direct component of the solar illumination, and the irradiance rapidly decreases until the entire cosine collector is shaded (point C_1). At point D_1, the band is no longer fully occluding the diffuser and direct sunlight begins to fall on a portion of the collector, so the irradiance increases. There is very little change in irradiance between points C_1 and D_1, because the width of the band is set to ensure a reasonable number of totally occluded data points are acquired. At point F_1, the band is horizontal and the instrument once again measures global irradiance. The time required for the band to move between points A_1 and F_1, which represents a full 180° swath, is 64 s.

5.6.1 Direct Irradiance Calculation

The main purpose of the BioSHADE accessory is to provide measurements of the optical properties of the atmosphere and, in particular, to allow the calculation of the direct-horizontal spectral irradiance (i.e., the irradiance on a horizontal plane from direct solar illumination), $E_b(0^+, \lambda, t)$. The calculation requires a variety of irradiance measurements made before, during, and after the passage of the shadowband over the cosine collector on the solar reference.

To calculate $E_b(0^+, \lambda, t)$, the solar zenith angle (θ) plus the following defined quantities are needed:

$E_n(0^+, \lambda, t)$ The direct-normal spectral irradiance (irradiance on a plane perpendicular to the detector–Sun direction).

$E_i(0^+, \lambda, t)$ The diffuse spectral irradiance (irradiance from the sky on a horizontal plane).

$E_d(0^+, \lambda, t)$ The global spectral irradiance (irradiance from the Sun and sky on a horizontal plane).

$E_k(0^+, \lambda, t_v)$ The hypothetical (i.e., it is not measured directly) spectral irradiance at the solar reference for the segment of the sky that is shaded by the shadowband at time t_v when the band is at shadowband angle v.

$E_p(0^+, \lambda, t_v)$ The spectral irradiance at the solar reference when the band is at shadowband angle v and not blocking direct sunlight.

$E_a(0^+, \lambda, t_v)$ The spectral irradiance at the solar reference when the centers of the solar disk, shadowband, and diffuser are aligned and direct sunlight is completely occluded.

$c_b(\lambda)$ The angular response error of the solar reference, defined as the ratio of angular response at incidence angle ϑ to $\cos(\vartheta)$.

$c_i(\lambda)$ The angular response error of the solar reference when exposed to isotropic radiation.

$c_d(\lambda)$ The angular response error of the solar reference when measuring global irradiance.

From these definitions, the following equations can be derived from inspection:

$$E_n(0^+,\lambda,t) = \frac{E_b(0^+,\lambda,t)}{\cos(\theta)}, \quad (6)$$

$$E_p(0^+,\lambda,t_v) = E_d(0^+,\lambda,t_v) - E_k(0^+,\lambda,t_v), \quad (7)$$

and

$$E_a(0^+,\lambda,t_v) = E_d(0^+,\lambda,t_v) - E_k(0^+,\lambda,t_v) - E_b(0^+,\lambda,t). \quad (8)$$

The six quantities $E_d(0^+,\lambda,t)$, $E_b(0^+,\lambda,t)$, $E_n(0^+,\lambda,t)$, $E_i(0^+,\lambda,t)$, $E_k(0^+,\lambda,t_v)$, $E_p(0^+,\lambda,t_v)$, and $E_a(0^+,\lambda,t_v)$ cannot be measured directly by the solar reference, because the solar reference is affected by a small angular response error (or *cosine error*). Quantities affected by this error are indicated by the prime symbol ($'$). For example, if the shadowband is below the horizon, the signal of the solar reference is proportional to $E'_d(0^+,\lambda,t) = c_G(\lambda)E_d(0^+,\lambda,t)$.

From (7) and (8), and the definition of $c_b(\lambda)$, it can be concluded that $E'_b(0^+,\lambda,t_M) = c_b(\lambda)E_b(0^+,\lambda,t_M) = E'_p(0^+,\lambda,t_M) - E'_a(0^+,\lambda,t_M)$, where t_M indicates the time when the centers of the Sun, shadowband, and collector are all aligned. This leads to the expression for the calculation of $E_b(0^+,\lambda,t_M)$:

$$E_b(0^+,\lambda,t_M) = \frac{E'_p(0^+,\lambda,t_M) - E'_a(0^+,\lambda,t_M)}{c_b(\lambda)}. \quad (9)$$

The challenge is that $E'_p(0^+,\lambda,t_M)$ is not directly accessible from the measurements acquired with the shadowband accessory, but must be extrapolated from observations taken at times when all parts of the collector are exposed to direct sunlight. (These are times to the left of point B_1 or to the right of point E_1 in Fig. 54).

To determine $E'_p(0^+,\lambda,t_M)$, an analysis software package was developed based on the formulation presented in (9). The software also determines performance metrics of the shadowband system, so the quality of the results can also be assessed. The software procedure that was developed is illustrated graphically in Fig. 55, which also indicates the relative change of the measured irradiance from one sample point to the next. This quantity is used to determine the times when the shadowband starts to shade the cosine collector from the direct illumination of sunlight (points B and E), and when the occlusion is at the maximum (point M).

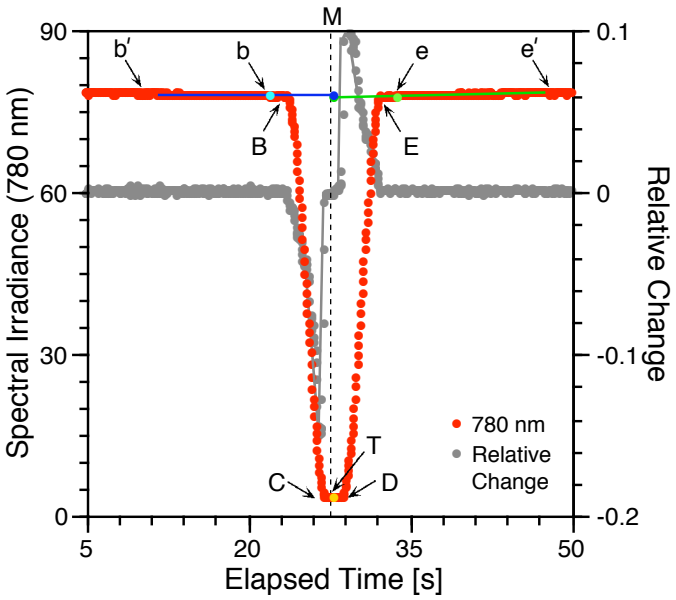

Fig. 55. A portion of the spectral irradiance at 780 nm from Fig. 54. The time M indicates when the centers of the Sun, shadowband, and collector were in line (as determined with the analysis software), and T is the intersection of the dashed line with spectral irradiance at 780 nm. The other points and the fitted lines are explained in the text.

A graphical depiction of the determination process for the $E'_p(0^+,\lambda,t_M)$ parameter is shown in Fig. 55. The $E'_p(0^+,\lambda,t_M)$ value (the blue circle on M near the top of the plot), is extrapolated via a linear regression using all measurements between points b′ and b. Additionally, $E'_p(0^+,\lambda,t_M)$ was extrapolated from measurements between points e and e′, as shown by the green circle, just below the blue circle, on M. The difference between the two extrapolated values, denoted $E'_{p_B}(0^+,\lambda,t_M)$ and $E'_{p_E}(0^+,\lambda,t_M)$, respectively, is a measure of the uncertainty for calculating $E'_p(0^+,\lambda,t_M)$ and presents the principal limitation of any shadowband approach for measuring $E_b(0^+,\lambda,t)$. As Fig. 55 indicates, the difference between $E'_{p_B}(0^+,\lambda,t_M)$ and $E'_{p_E}(0^+,\lambda,t_M)$ is rather small. The difference tends to be larger at shorter wavelengths, however, because of the larger values of $E_k(0^+,\lambda,t_v)$ and their dependence on the band position.

The variation of $E'_{p_B}(0^+,\lambda,t_M)$ and $E'_{p_E}(0^+,\lambda,t_M)$ at $\lambda = 780$ nm was investigated for several consecutive shading events during stable atmospheric conditions. The relative difference was on the order of 0.2%. The average of the two values exhibited little *noise*, from one event to the next. Consequently, this value was used for the calculations of $E_b(0^+,\lambda,t)$ presented below. A similar analysis was performed for $\lambda = 320$ nm, for which the relative difference was typically 1.5%, but the average of the two extrapolated values varied by less than 0.3% from one shading event to the next. This suggests $E'_p(0^+,\lambda,t_M)$ can be calculated from all spectral channels with high accuracy.

5.6.2 Shaded Irradiance

The accurate determination of the $E'_a(0^+, \lambda, t_M)$ parameter is also required for the calculation of $E_b(0^+, \lambda, t)$. The value $E'_a(0^+, \lambda, t_M)$ is defined here as the average of all sample points between points C and D, where the relative point-to-point change is less than 0.2% (see Fig. 55 for the definition of points C and D). The number of points contributing to this average is shown in Fig. 56 for measurements on 7 October 2008 performed for SZA values from 33–85°. The number of points increases with SZA. This can be explained as follows: the axis of the shadowband was approximately oriented in the East–West direction. At a large SZA (or close to sunrise and sunset), the Sun is either in the East or West. In this case, the angular movement of the band across the disk of the Sun is slower than when the axis is perpendicular to the line of the collector and Sun, explaining the large number of sample points contributing to $E'_a(0^+, \lambda, t_M)$.

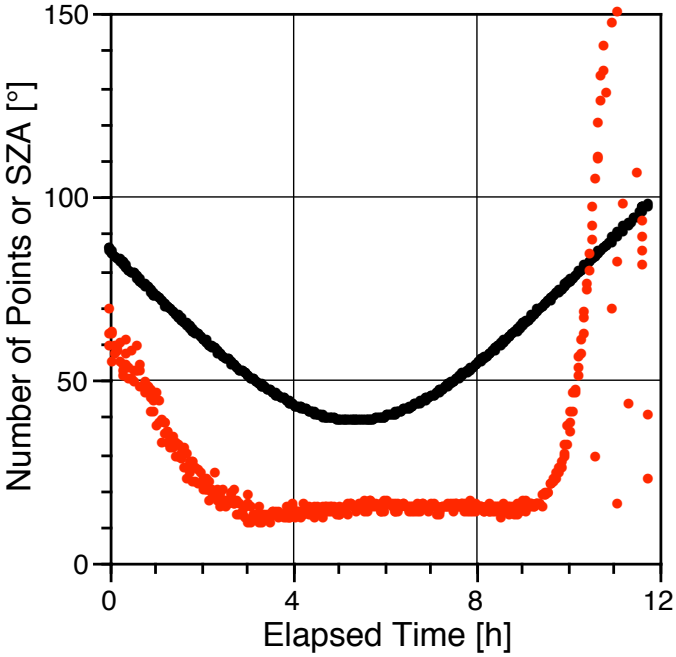

Fig. 56. The number of data points (red) contributing to the $E'_a(0^+, \lambda, t_M)$ values as a function of SZA (black). The two parameters share the same axis, but with different units.

The ability of the system to determine $E'_a(0^+, \lambda, t_M)$ with high confidence was estimated by analyzing a time series of $E'_a(0^+, \lambda, t_M)$ over several shading events (results are presented in Fig. 57). At 320 nm, there is virtually no event-to-event variation beyond the upward slope resulting from the decrease of SZA during the evaluation period. At 780 nm there is some variation, which is likely partly due to real changes of the atmosphere (e.g., change in aerosol loading); however, the event-to-event variation at this wavelength is also smaller than 0.7%.

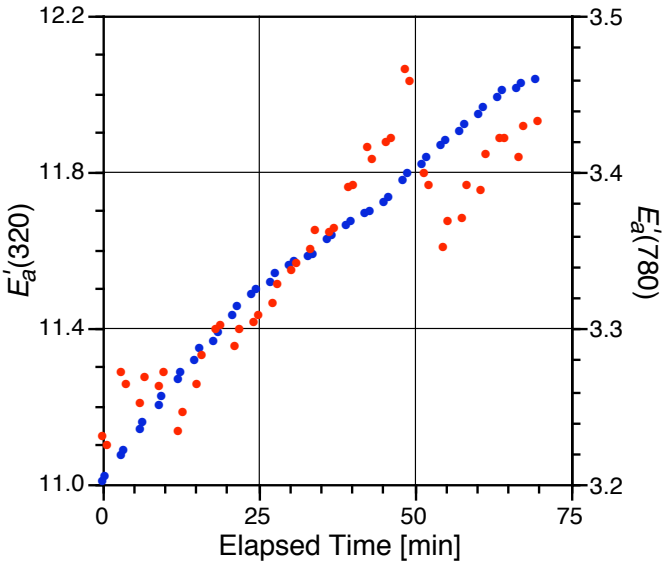

Fig. 57. Measurements of $E'_a(0^+, \lambda, t_M)$ at 780 and 320 nm (red and blue, respectively).

Figure 58 shows the diurnal cycle of $E'_a(0^+, \lambda, t_M)$ for all 19 wavelengths of BioSHADE. There is some asymmetry, with lower values generally in the morning, indicating that the atmosphere's aerosol loading has changed over the course of the day. The largest spectral irradiance is observed at 412 nm. Measurements at wavelengths larger than 600 nm are comparatively low because the largest contribution stems from direct irradiance, which is blocked.

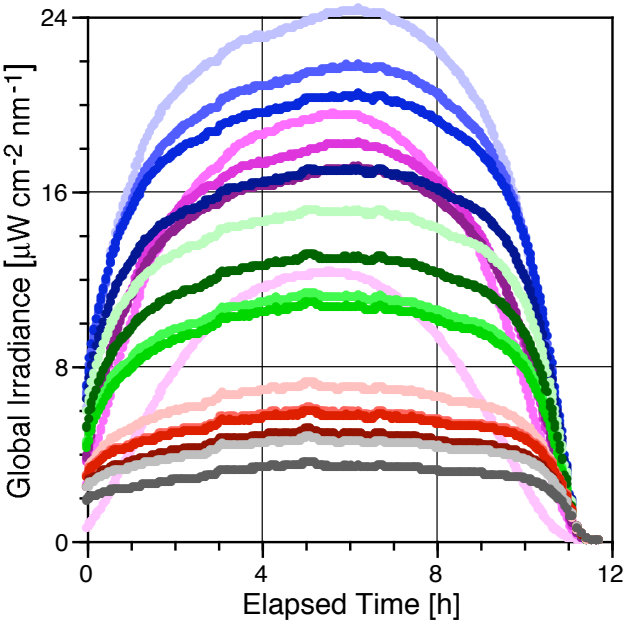

Fig. 58. Measurements of $E'_a(0^+, \lambda, t_M)$ using the following gradient (respectively): light-to-dark violet 320, 340, 380, 395 nm; light-to-dark blue 412, 443, 465, and 490 nm; light-to-dark green 510, 532, 555, and 560 nm; light-to-dark red 625, 665, 670, and 683 nm; and light and dark gray 710 and 780 nm.

5.6.3 Direct Normal Irradiance

Figure 59 shows the diurnal variation of direct-normal irradiance $E_n(0^+, \lambda, t_M)$ calculated using (6). Data are not perfectly symmetrical about the solar noon, most probably due to changes in aerosol loading over the course of the day. There is a "hump" in data measured at SZA larger than 80° at wavelengths larger than 600 nm. This feature is likely related to an incomplete correction of the system's cosine error. (At the time of this analysis, a detailed cosine correction of the instrument was not yet available; the cosine correction used was based on a generic function for microradiometers, which may not be appropriate for this particular instrument at long wavelengths.)

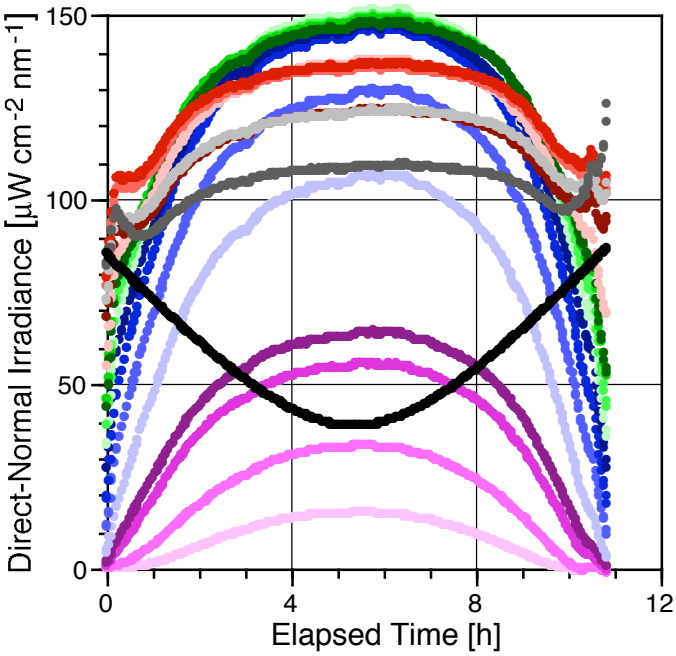

Fig. 59. Spectral direct-normal irradiance for 7 October 2008. The SZA is shown in black using the y-axis numerical values, but in degrees.

5.6.4 Global Irradiance

Figure 60 shows the diurnal variation of cosine-error corrected global irradiance, $E_d(0^+, \lambda, t)$, measured at times associated with points G_1, G_2, and G_3 (Fig. 54 defines the latter three points). The value $E_d(0^+, \lambda, t)$ was calculated from uncorrected global irradiance data $E'_d(0^+, \lambda, t)$ using the following formulation:

$$E_d(0^+, \lambda, t) = \Big[E'_d(0^+, \lambda, t) - c_b E_b(0^+, \lambda, t) + c_i E_b(0^+, \lambda, t)\Big] c_i^{-1}, \quad (10)$$

where the angular response error terms are from Sect. 5.6.1. Values of $E_b(0^+, \lambda, t)$ in (10) were interpolated from $E_b(0^+, \lambda, t_M)$ to the times associated with points G_i.

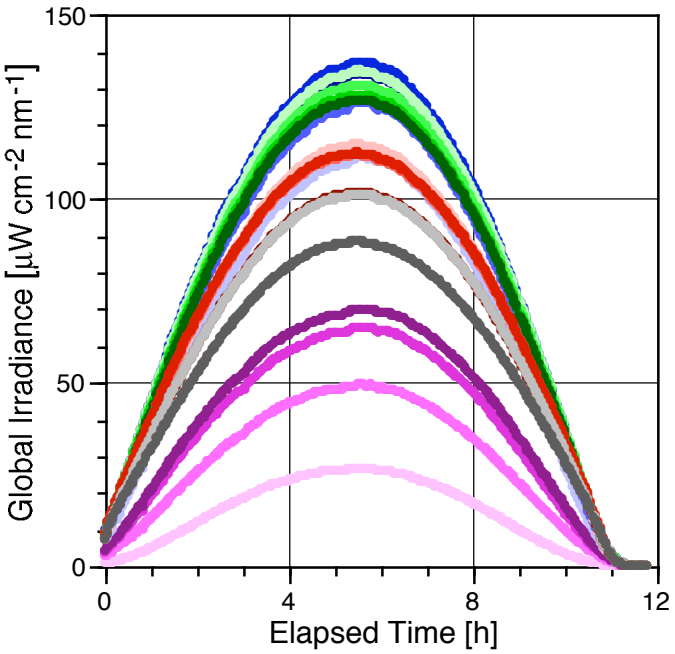

Fig. 60. Spectral global irradiance $E_d(0^+, \lambda, t)$ for 7 October 2008. A cosine-error correction was applied.

5.6.5 Langley Plots

The change of direct-normal irradiance with SZA is determined by the Beer–Lambert's law:

$$E_n(0^+, \lambda, t) = E_0(\lambda, t) \exp^{-\tau(\lambda) m(\theta)}, \quad (11)$$

where $E_0(\lambda, t)$ is the direct-normal irradiance outside Earth's atmosphere, $\tau(\lambda)$ is the spectral optical depths of all scatters and absorbers in the atmosphere, and $m(\theta)$ is the relative optical airmass, which is a function of SZA and can be approximated with:

$$m(\theta) = \left[\cos(\theta) + 0.50572\,(96.07995 - \theta)^{-1.6364}\right]^{-1}. \quad (12)$$

Taking the logarithm of (11) leads to:

$$\ln[E_n(0^+, \lambda, t)] = \ln[E_0(\lambda, t)] - \tau(\lambda) m(\theta). \quad (13)$$

If $\tau(\lambda)$ does not change over the course of the day, $\ln[E_n(0^+, \lambda, t)]$ becomes a linear function of $m(\theta)$. Plotting measured data of $\ln[E_n(0^+, \lambda, t)]$ versus $m(\theta)$ allows for the determination of $E_0(\lambda, t)$ by extrapolation to $m(\theta) = 0$, and to estimate $\tau(\lambda)$. The optical depth $\tau(\lambda)$ is the sum of the Rayleigh optical depth $\tau_R(\lambda)$, aerosol optical depth $\tau_A(\lambda)$, and the optical depth $\tau_X(\lambda)$ of other scatterers and absorbers. By calculating $\tau_R(\lambda)$ and $\tau_X(\lambda)$, the aerosol optical depth $\tau_A(\lambda)$ can be determined. Plots of $E_n(0^+, \lambda, t)$ versus $m(\theta)$ are known as Langley plots.

Langley plots from irradiance data collected with the BioSHADE accessory were used to determine the potential for deriving $E_0(\lambda, t)$ and $\tau_A(\lambda)$. A Langley plot for

data measured on 7 October 2008 is presented in Fig. 61, which shows $\ln[E_n(0^+, \lambda, t)]$ varies fairly linearly with airmass $m(\theta)$ for $m(\theta) < 3$ (where θ is less than 70°) with similar values in the morning and afternoon, as expected. For an airmass between 3–8 (where θ is between 70° and 82°), measurements made in the afternoon are lower (measurements at 320 nm and 340 nm are below the detection limit). For even higher airmass values, the pattern reverses. These variations are likely caused by changes in aerosol loading throughout the day, but could also be caused by systematic instrument errors.

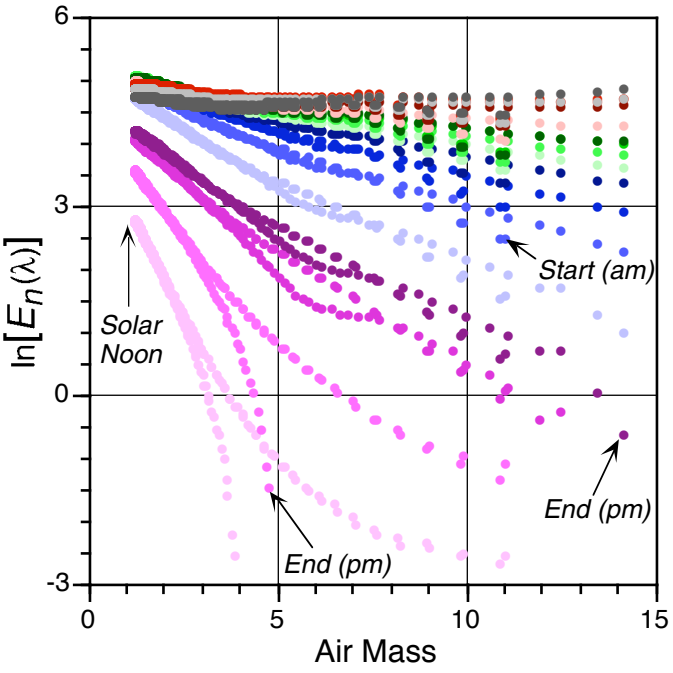

Fig. 61. A Langley plot for data measured on 7 October 2008 using the same spectral correspondence for the colored symbols that was established for Fig. 58.

5.7 Summary

Analysis of BioSHADE data has confirmed that the instrument meets its design specifications. The number of sample points recorded while the shadowband is completely blocking the Sun is sufficient for accurate retrievals of $E_a(0^+, \lambda, t_M)$. Furthermore, $E_p(0^+, \lambda, t_M)$ can be accurately determined by extrapolating measurements taken immediately before and after the times when the shadowband starts to cast a shadow of the Sun on the instrument's collector. Precise knowledge of $E_a(0^+, \lambda, t_M)$ and $E_p(0^+, \lambda, t_M)$ allows for the direct-horizontal and direct-normal irradiance to be calculated with confidence, and to construct Langley plots. The instrument size and recording speed also meet specifications.

The GPS unit provides UTC, longitude, and latitude every second. These parameters are fully integrated into the data stream of the microradiometer system and available for processing. This ensures that proper record traceability exists for sampling times and station position during data acquisition. Although not common, it is not unheard of for a research vessel to have GPS problems, so a redundant data stream can be very useful. The latter is particularly true for calibration and validation exercises wherein an important objective is to provide matchups between the *in situ* and remote sensing observations. In addition, many small vessels do not automatically record position as a function of time or have displays located where scientific work is being done, because of space and resource limitations.

The BioSHADE and BioGPS systems can be fully integrated with instrumentation based on the microradiometer architecture, wherein the two devices are operated over a single cable, linking radiometers, BioGPS, and the BioSHADE accessory. The latter ensures the accessory components and the radiometric sensors can be operated using standard cabling and deck box configurations.

Acknowledgments

The success of the data acquisition and data processing capabilities presented here would not have been possible without funding support from the NASA OBB Program Office. The microradiometer, aggregator, and associated systems were developed by Biospherical Instruments, Inc., with funding from the NASA SBIR Program under contract NNG06CA03C entitled "*In Situ* Radiometers: Smaller, Faster, and Scalable to Hyperspectral." The preparation of the manuscript and its final level of completeness benefitted significantly from the technical editing expertise of Elaine Firestone whose attentiveness to detail, and good cheer, are greatly appreciated.

Glossary

3GμR	Three-Gain Microradiometer
A/D	Analog-to-Digital
ADC	Analog-to-Digital Converter
AERONET	Aerosol Robotic Network
AOI	Angle of Incidence
AOPs	Apparent Optical Properties
ASCII	American Standard Code for Information Interchange
AWG	American Wire Gauge
BATS	Bermuda Atlantic Time Series
BioGPS	Biospherical Global Positioning System
BioOPS	Biospherical Optical Profiling System
BioPRO	Biospherical Profiler
BioSHADE	Biospherical Shadowband Accessory for Diffuse Irradiance
BioSOPE	Biogeochemistry and Optics South Pacific Experiment
BioSORS	Biospherical Surface Ocean Reflectance System
BOUSSOLE	*Bouée pour l'acquisition de Séries Optiques à Long Terme* (literally translated from French as the "buoy for the acquisition of a long-term optical series.")
CCGS	Canadian Coast Guard Ship
CCW	Counterclockwise
CDR	Climate-quality Data Record
CERBERUS	Compact Environmental Radiometer Buoyancy Enhancements for Rate-Adjusted Underwater Sampling
C-HOIST	Cable Hauler for Optical *In Situ* Technologies
C-OPS	Compact-Optical Profiling System
COTS	Commercial Off-The-Shelf
CSTARS	Center For Southeastern Tropical Advanced Remote Sensing
CVO	Calibration and Validation Office
CW	Clockwise
DARR-94	The first SeaWiFS Data Analysis Round Robin
DARR-00	The second SeaWiFS Data Analysis Round Robin
EOS	Earth Observing System
EPIC	Enhanced Performance Instrument Class
FAFOV	Full-Angle Field of View
FEL	Not an acronym, but a lamp designator.
FPA	Filter-Photodetector Assemblies
FOV	Field of View
FWHM	Full Width at Half Maximum
GPS	Global Positioning System
GSFC	Goddard Space Flight Center
HD	Housing Diameter
ICESCAPE	Impacts of Climate on Ecosystems and Chemistry of the Arctic Pacific Environment
IOPs	Inherent Optical Properties
IR	Infrared
LCD	Liquid Crystal Display
LED	Light Emitting Diode
LoCNESS	Low-Cost NASA Environmental Sampling System
LOV	*Laboratoire d'Océanographie de Villefranche*
MERIS	Medium Resolution Imaging Spectrometer
microSAS	micro-Surface Acquisition System
microSD	Microsecure Digital (card)
microNESS	micro-NASA Environmental Sampling System
miniNESS	miniature NASA Environmental Sampling System
MMS	Multiple Microradiometer System
MOBY	Marine Optical Buoy
MODIS	Moderate Resolution Imaging Spectroradiometer
MODIS-A	Moderate Resolution Imaging Spectroradiometer-Aqua
MODIS-T	Moderate Resolution Imaging Spectroradiometer-Terra
NASA	National Aeronautics and Space Administration
NEI	Noise Equivalent Irradiance
NER	Noise Equivalent Radiance
NIR	Near Infrared
NIST	National Institute of Standards and Technology
NMEA	National Marine Electronics Association
NPT	National Pipe Tapered
OBB	Ocean Biology and Biogeochemistry
OCTS	Ocean Color and Temperature Scanner
OSPREy	Optical Sensors for Planetary Radiant Energy
OXR	OSPREy Transfer Radiometer
PAR	Photosynthetically Available Radiation
PCA	Printed Circuit Assembly
PE	Polyethylene
PGA	Programmable Gate Array
POLDER	Polarization and Directionality of the Earth's Reflectance
PP	Polypropylene
PRR	Profiling Reflectance Radiometer
psia	Pressure per Square Inch Absolute
PU	Polyurethane
PURLS	Portable Universal Radiometer Light Source
QA	Quality Assurance
RPD	Relative Percent Difference
RSMAS	Rosenstiel School of Marine and Atmospheric Science
RTD	Resistance Temperature Detector
R/V	Research Vessel

SAS	Surface Acquisition System
SBIR	Small Business Innovation Research
SeaBASS	SeaWiFS Bio-optical Archive and Storage System
SeaFALLS	SeaWiFS Free-Falling Advanced Light Level Sensors
SeaPRISM	SeaWiFS Photometer Revision for Incident-Surface Measurements
SeaSAS	SeaWiFS Surface Acquisition System
SeaWiFS	Sea-viewing Wide Field-of-view Sensor
SHALLO	Scalable Hydro-optical Applications for Light-Limited Oceanography
SIRREX	SeaWiFS Intercalibration Round-Robin Experiment
SPI	Serial Peripheral Interface
SPMR	SeaWiFS Profiling Multichannel Radiometer
SQM	SeaWiFS Quality Monitor
SS	Stainless Steel
STAR	Standardized Technologies for Applied Radiometry
SuBOPS	Submersible Biospherical Optical Profiling System
SUnSAS	SeaWiFS Underway Surface Acquisition System
SWIR	Short-Wave Infrared
SZA	Solar Zenith Angle
T-MAST	Telescoping Mount for Advanced Solar Technologies
UAV	Unmanned Aerial Vehicle
UPD	Unbiased Percent Difference
USB	Universal Serial Bus
USCGC	United States Coast Guard Cutter
UTC	Universal Time Coordinated
UV	Ultraviolet
XTRA	Expandable Technologies for Radiometric Applications

Symbols

C_a	Chlorophyll a concentration.
$c_b(\lambda)$	The angular response error of the solar reference.
$C_c(\lambda)$	The spectral calibration coefficient.
$c_d(\lambda)$	The angular response error of the solar reference when measuring global irradiance.
$c_i(\lambda)$	The angular response error of the solar reference when exposed to isotropic radiation.
d	The distance between the lamp and the diffuser faceplate.
$\bar{D}(\lambda)$	The average bias or dark voltage.
$E(\lambda)$	Spectral irradiance.
$E(z,\lambda)$	Spectral irradiance at a depth z.
$E(0^+,\lambda)$	The in-air spectral irradiance just above the sea surface.
$E(0^-,\lambda)$	The in-water spectral irradiance at null depth ($z = 0^-$).
$E_0(\lambda)$	The direct-normal spectral irradiance outside the Earth's atmosphere (irradiance on a plane perpendicular to the detector–Sun direction).
$E_a(0^+,\lambda)$	The spectral irradiance at the solar reference when the centers of the solar disk, shadowband, and diffuser are aligned and direct sunlight is completely occluded (at time t_υ).
$E_b(0^+,\lambda)$	The direct-horizontal spectral irradiance (irradiance on a horizontal plane from direct solar illumination).
$E_{\mathrm{cal}}(\lambda,t_i)$	The spectral calibrated irradiance.
$E_d(z,\lambda)$	The in-water spectral downward irradiance profile.
$E_d(0^+,\lambda)$	The spectral global solar irradiance (from the Sun and sky on a horizontal plane).
$E_d^B(0^+,\lambda)$	The global solar irradiance measured by a bow sensor.
$E_d^S(0^+,\lambda)$	The global solar irradiance measured by a stern sensor.
$E_i(0^+\lambda)$	The spectral diffuse (sky) irradiance (irradiance from the sky on a horizontal plane).
$E_k(0^+,\lambda)$	The hypothetical spectral irradiance at the solar reference for the segment of the sky that is shaded by the shadowband when the band is at time t_υ and the shadowband is at angle υ.
$E_n(0^+,\lambda)$	The direct-normal spectral irradiance (irradiance on a plane perpendicular to the detector–Sun direction).
$E_p(0^+,\lambda)$	The spectral irradiance at the solar reference at time t_υ when the band is at shadowband angle υ and not blocking direct sunlight.
$E'_{p_B}(0^+,\lambda)$	An extrapolated spectral irradiance (at the solar reference) at time t_M using an interval denoted B.
$E'_{p_E}(0^+,\lambda)$	An extrapolated spectral irradiance (at the solar reference) at time t_M using an interval denoted E.
E_s	A solar reference sensor.
$I_f(\lambda)$	The spectral immersion factor.
$K(\lambda)$	The spectral diffuse attenuation coefficient.
$K_d(\lambda)$	The spectral diffuse attenuation coefficient computed from $E_d(z,\lambda)$.
$L_i(0^+,\lambda)$	The spectral indirect (or sky) radiance reaching the sea surface.
$L_p(0^+,\lambda)$	The radiance of the plaque.
$L_T(0^+,\lambda)$	The (total) radiance above the sea surface.
$L_u(\lambda)$	The upwelled spectral radiance.
$L_u(z,\lambda)$	The upwelled spectral radiance at depth z.
$L_W(\lambda)$	The spectral radiance leaving the sea surface from below (the water-leaving radiance).
$\hat{L}_W(\lambda)$	The spectral water-leaving radiance derived from an above-water sampling method.
$\tilde{L}_W(\lambda)$	The spectral water-leaving radiance derived from an in-water sampling method.
$[L_W(\lambda)]_{\mathrm{N}}$	The spectral normalized water-leaving radiance.
M	The point (in time) when the centers of the Sun, shadowband, and collector are all aligned.
$m(\theta)$	The relative optical airmass.
N_P	The number of photodetectors.
$n_w(\lambda)$	The spectral refractive index of water, which is also a function of S and T.
$\mathfrak{P}$	The in-water radiometric quantities in physical units (L_u, E_d, or E_u).
P_e	The packing efficiency of microradiometers into a cylinder.
$\mathfrak{P}(z,\lambda,t_0)$	A radiometric parameter (L_u, E_d, or E_u) as it would have been recorded at all depths z at the same time t_0.
$\mathfrak{P}(0^-,\lambda)$	A subsurface radiometric quantity (L_u, E_d, or E_u) at null depth $z = 0^-$.
Q_n	Nadir-viewing measurements.

R_d Radius of the diffuser.
$R_{\rm rs}$ Remote sensing reflectance.
$\Re$ The effects of reflection and refraction.
$\Re_0$ The $\Re$ term evaluated at nadir, i.e., $\theta' = 0$
S Salinity.
t Time.
T Water temperature.
t_0 A reference time (generally chosen to coincide with the start of a measurement sequence).
t_i A specific time.
$T_s(\lambda)$ The spectral transmittance of the water surface to downward irradiance.
t_υ The time when the shadowband is at angle υ.
$V(\lambda, t_i)$ Spectral digitized voltages (in counts).
W Wind speed.
x The horizontal axis (abscissa).
X An arbitrary reference measurement.
Y An arbitrary measurement to be investigated.
z The vertical (depth) coordinate, where the depth is the height of water above the cosine collectors.
z_c The critical depth.
θ Solar zenith angle.
θ' The above-water viewing angle (ϑ) refracted by the air–sea interface.
ϑ The radiometer pointing angle with respect to the vertical axis, z.
ϑ' The angle ϑ measured with respect to the zenith.
λ Wavelength.
ρ The surface reflectance factor.
$\tau(\lambda)$ The spectral optical depths of all scatters and absorbers in the atmosphere.
$\tau_A(\lambda)$ The aerosol optical depth.
$\tau_R(\lambda)$ The Rayleigh optical depth.
$\tau_X(\lambda)$ Other scatters and absorbers at optical depth.
ϕ The solar azimuth angle.
φ The perturbations (or tilts) in vertical alignment, which can change the pointing angles.
ϕ' An angle away from the Sun (here either 90° or 135°).
ϕ^- An angle 90° counterclockwise away from the Sun.
ϕ^+ An angle 90° clockwise away from the Sun.
ψ The RPD value.

References

Antoine, D., F. d'Ortenzio, S.B. Hooker, G. Bécu, B. Gentili, D. Tailliez, and A.J. Scott, 2008: Assessment of uncertainty in the ocean reflectance determined by three satellite ocean color sensors (MERIS, SeaWiFS and MODIS-A) at an offshore site in the Mediterranean Sea (BOUSSOLE project). *J. Geophys. Res.,* **113,** C07013, doi:10.1029/2007JC004472, 2008.

Austin, R.W., 1974: "The Remote Sensing of Spectral Radiance from Below the Ocean Surface." In: *Optical Aspects of Oceanography,* N.G. Jerlov and E.S. Nielsen, Eds., Academic Press, London, 317–344.

Bailey, S.W., S.B. Hooker, D. Antoine, B.A. Franz, P.J. Werdell, 2008: Sources and assumptions for the vicarious calibration of ocean color satellite observations. *Appl. Opt.,* **47,** 2,035–2,045.

Booth, C.R., T. Mestechkina, and J.H. Morrow, 1994: Errors in the reporting of solar spectral irradiance using moderate bandwidth radiometers: an experimental investigation. *SPIE Ocean Optics XII,* **2258,** 654–662.

Carder, K.L., and R.G. Steward, 1985: A remote sensing reflectance model of a red tide dinoflagellate off West Florida. *Limnol. Oceanogr.,* **30,** 286–298.

Clark, D., H.R. Gordon, K.J. Voss, Y. Ge, W. Broenkow, and C. Trees, 1997: Validation of atmospheric correction over the oceans. *J. Geophys. Res.,* **102,** 17,209–17,217.

Claustre, H., A. Sciandra, and D. Vaulot, 2008: Introduction to the special section bio-optical and biogeochemical conditions in the South East Pacific in late 2004: The BIOSOPE program. *Biogeosci.,* **5,** 679–691.

Doyle, P.J., S.B. Hooker, G. Zibordi, and D. van der Linde, 2003: Validation of an In-Water, Tower-Shading Correction Scheme. *NASA Tech. Memo. 2003–206892, Vol. 25,* S.B. Hooker and E.R. Firestone, Eds., NASA Goddard Space Flight Center, Greenbelt, Maryland, 32 pp.

Fougnie, B., R. Frouin, P. Lecomte, and P-Y. Deschamp, 1999: Reduction of skylight reflection effects in the above-water measurement of diffuse marine reflectance. *Appl. Opt.,* **38,** 3,844–3,856.

Gordon, H.R., and D.K. Clark, 1981: Clear water radiances for atmospheric correction of coastal zone color scanner imagery. *Appl. Opt.,* **20,** 4,175–4,180.

——, and K. Ding, 1992: Self-shading of in-water optical instruments. *Limnol. Oceanogr.,* **37,** 491–500.

Holben, B.N., T.F. Eck, I. Slutsker, D. Tanré, J.P. Buis, A. Setzer, E. Vermote, J.A. Reagan, Y.J. Kaufman, T. Nakajima, F. Lavenu, I. Jankowiak, and A. Smirnov, 1998: AERONET—A federated instrument network and data archive for aerosol characterization. *Remote Sens. Environ.,* **66,** 1–16.

Hooker, S.B., 2000: "Stability Monitoring of Field Radiometers Using Portable Sources." In: G.S. Fargion and J.L. Mueller, Ocean Optics Protocols for Satellite Ocean Color Sensor Validation, Revision 2. *NASA Tech. Memo. 2000–209966,* NASA Goddard Space Flight Center, Greenbelt, Maryland, 57–64.

——, 2002: "Stability Monitoring of Field Radiometers Using Portable Sources." In: Mueller, J.L., and 39 Co-authors, Ocean Optics Protocols for Satellite Ocean Color Sensor Validation, Revision 3, Volume 1, J.L. Mueller and G.S. Fargion, Eds., *NASA Tech. Memo. 2002–210004/Rev3/Vol1,* NASA Goddard Space Flight Center, Greenbelt, Maryland, 91–99.

——, and W.E. Esaias, 1993: An overview of the SeaWiFS project. *Eos, Trans., Amer. Geophys. Union,* **74,** 241–246.

——, and J. Aiken, 1998: Calibration evaluation and radiometric testing of field radiometers with the SeaWiFS Quality Monitor (SQM). *J. Atmos. Oceanic Tech.,* **15,** 995–1,007.

——, G. Zibordi, G. Lazin, and S. McLean, 1999: The SeaBOARR-98 Field Campaign. *NASA Tech. Memo. 1999–206892, Vol. 3,* S.B. Hooker and E.R. Firestone, Eds., NASA Goddard Space Flight Center, Greenbelt, Maryland, 40 pp.

——, and G. Lazin, 2000: The SeaBOARR-99 Field Campaign. *NASA Tech. Memo. 2000–206892, Vol. 8,* S.B. Hooker and E.R. Firestone, Eds., NASA Goddard Space Flight Center, 46 pp.

——, and S. Maritorena, 2000: An evaluation of oceanographic radiometers and deployment methodologies. *J. Atmos. Oceanic Technol.,* **17,** 811–830.

——, and C.R. McClain, 2000: The calibration and validation of SeaWiFS data. *Prog. Oceanogr.,* **45,** 427–465.

——, and A. Morel, 2003: Platform and environmental effects on above- and in-water determinations of water-leaving radiances. *J. Atmos. Ocean. Technol.,* **20,** 187–205.

——, and G. Zibordi, 2005: Platform perturbations in above-water radiometry. *Appl. Opt.,* **44,** 553–567.

——, H. Claustre, J. Ras, L. Van Heukelem, J-F. Berthon, C. Targa, D. van der Linde, R. Barlow, and H. Sessions, 2000a: The First SeaWiFS HPLC Analysis Round-Robin Experiment (SeaHARRE-1). *NASA Tech. Memo. 2000–206892, Vol. 14,* S.B. Hooker and E.R. Firestone, Eds., NASA Goddard Space Flight Center, Greenbelt, Maryland, 42 pp.

——, G. Zibordi, J-F. Berthon, S.W. Bailey, and C.M. Pietras, 2000b: The SeaWiFS Photometer Revision for Incident Surface Measurement (SeaPRISM) Field Commissioning. *NASA Tech. Memo. 2000–206892, Vol. 13,* S.B. Hooker and E.R. Firestone, Eds., NASA Goddard Space Flight Center, Greenbelt, Maryland, 24 pp.

——, ——, ——, D. D'Alimonte, S. Maritorena, S. McLean, and J. Sildam, 2001: Results of the Second SeaWiFS Data Analysis Round Robin, March 2000 (DARR-00). *NASA Tech. Memo. 2001–206892, Vol. 15,* S.B. Hooker and E.R. Firestone, Eds., NASA Goddard Space Flight Center, Greenbelt, Maryland, 71 pp.

——, S. McLean, J. Sherman, M. Small, G. Lazin, G. Zibordi, and J.W. Brown, 2002a: The Seventh SeaWiFS Intercalibration Round-Robin Experiment (SIRREX-7), March 1999. *NASA Tech. Memo. 2002–206892, Vol. 17,* S.B. Hooker and E.R. Firestone, Eds., NASA Goddard Space Flight Center, Greenbelt, Maryland, 69 pp.

——, G. Lazin, G. Zibordi, and S. McLean. 2002b. An evaluation of above- and in-water methods for determining water-leaving radiances. *J. Atmos. Oceanic Technol.,* **19,** 486–515.

——, G. Zibordi, J-F. Berthon, D. D'Alimonte, D. van der Linde, and J.W. Brown, 2003: Tower-Perturbation Measurements in Above-Water Radiometry. *NASA Tech. Memo. 2003–206892, Vol. 23,* S.B. Hooker and E.R. Firestone, Eds., NASA Goddard Space Flight Center, Greenbelt, Maryland, 35 pp.

——, ——, ——, and J.W. Brown, 2004: Above-water radiometry in shallow, coastal waters. *Appl. Opt.,* **43,** 4,254–4,268.

——, L. Van Heukelem, C.S. Thomas, H. Claustre, J. Ras, L. Schlüter, J. Perl, C. Trees, V. Stuart, E. Head, R. Barlow, H. Sessions, L. Clementson, J. Fishwick, C. Llewellyn, and J. Aiken, 2005: The Second SeaWiFS HPLC Analysis Round-Robin Experiment (SeaHARRE-2). *NASA Tech. Memo. 2005–212785,* NASA Goddard Space Flight Center, Greenbelt, Maryland, 112 pp.

——, ——, ——, ——, ——, ——, L. Clementson, D. Van der Linde, E. Eker-Develi, J-F. Berthon, R. Barlow, H. Sessions, J. Perl, and C. Trees, 2009: The Third SeaWiFS HPLC Analysis Round-Robin Experiment (SeaHARRE-3). *NASA Tech. Memo. 2009,* NASA Goddard Space Flight Center, Greenbelt, Maryland, 97 pp.

——, G. Bernhard, J.H. Morrow, C.R. Booth, T. Cromer, R.N. Lind, and V. Quang, 2010: Optical Sensors for Planetary Radiant Energy (OSPREy): Calibration and Validation of Current and Next-Generation NASA Missions. *NASA Tech. Memo.,* NASA Goddard Space Flight Center, Greenbelt, Maryland, (in prep.).

Johnson, B.C., S.S. Bruce, E.A. Early, J.M. Houston, T.R. O'Brian, A. Thompson, S.B. Hooker, and J.L. Mueller, 1996: The Fourth SeaWiFS Intercalibration Round-Robin Experiment (SIRREX-4), May 1995. *NASA Tech. Memo. 104566, Vol. 37,* S.B. Hooker and E.R. Firestone, Eds., NASA Goddard Space Flight Center, Greenbelt, Maryland, 65 pp.

——, F. Sakuma, J.J. Butler, S.F. Biggar, J.W. Cooper, J. Ishida, and K. Suzuki, 1997: Radiometric Measurement Comparison Using the Ocean Color Temperature Scanner (OCTS) Visible and Near Infrared Integrating Sphere. *J. Res. NIST,* **102,** 627–646.

——, P-S. Shaw, S.B. Hooker, and D. Lynch, 1998: Radiometric and engineering performance of the SeaWiFS Quality Monitor (SQM): A portable light source for field radiometers. *J. Atmos. Oceanic Tech.,* **15,** 1,008–1,022.

——, H.W. Yoon, S.S. Bruce, P-S. Shaw, A. Thompson, S.B. Hooker, R.E. Eplee, Jr., R.A. Barnes, S. Maritorena, and J.L. Mueller, 1999: The Fifth SeaWiFS Intercalibration Round-Robin Experiment (SIRREX-5), July 1996. *NASA Tech. Memo. 1999–206892, Vol. 7,* S.B. Hooker and E.R. Firestone, Eds., NASA Goddard Space Flight Center, 75 pp.

McClain, C.R., W.E. Esaias, W. Barnes, B. Guenther, D. Endres, S.B. Hooker, G. Mitchell, and R. Barnes, 1992: Calibration and Validation Plan for SeaWiFS. *NASA Tech. Memo. 104566, Vol. 3,* S.B. Hooker and E.R. Firestone, Eds., NASA Goddard Space Flight Center, Greenbelt, Maryland, 41 pp.

——, G.C. Feldman, and S.B. Hooker, 2004: An overview of the SeaWiFS project and strategies for producing a climate research quality global ocean bio-optical time series. *Deep Sea Res. II,* **51,** 5–42.

Mobley, C.D., 1999: Estimation of the remote-sensing reflectance from above-surface measurements. *Appl. Opt.,* **38,** 7,442–7,455.

Morel, A., and L. Prieur, 1977: Analysis of variations in ocean color. *Limnol. Oceanogr.,* **22,** 709–722.

——, and B. Gentili, 1996: Diffuse reflectance of oceanic waters, III. Implication of bidirectionality for the remote sensing problem. *Appl. Opt.,* **35,** 4,850–4,862.

——, and J.L. Mueller, 2002: "Normalized Water-Leaving Radiance and Remote Sensing Reflectance: Bidirectional Reflectance and Other Factors." In: J.L. Mueller and G.S. Fargion, Ocean Optics Protocols for Satellite Ocean Color Sensor Validation, Revision 3, Volume 2. *NASA Tech. Memo. 2002–210004/Rev3–Vol2,* NASA Goddard Space Flight Center, Greenbelt, Maryland, 183–210.

Morrow, J.H., M.S. Duhig, C.R. Booth, 1994: Design and evaluation of a cosine collector for a SeaWiFS-compatible marine reflectance radiometer. *SPIE Ocean Optics XII,* **2258,** 879–886.

——, M. Duhig, and C.R. Booth, 1994: Design and Evaluation of a cosine collector for a SeaWiFS-compatible Marine Reflectance Radiometer. *SPIE Ocean Optics XII,* **2258,** 879–886.

Mueller, J.L., 1993: The First SeaWiFS Intercalibration Round-Robin Experiment, SIRREX-1, July 1992. *NASA Tech. Memo. 104566, Vol. 14,* S.B. Hooker and E.R. Firestone, Eds., NASA Goddard Space Flight Center, Greenbelt, Maryland, 60 pp.

——, 1995: "Comparison of Irradiance Immersion Coefficients for Several Marine Environmental Radiometers (MERs)." In: Mueller, J.L., R.S. Fraser, S.F. Biggar, K.J. Thome, P.N. Slater, A.W. Holmes, R.A. Barnes, C.T. Weir, D.A. Siegel, D.W. Menzies, A.F. Michaels, and G. Podesta: Case Studies for SeaWiFS Calibration and Validation, Part 3. *NASA Tech. Memo. 104566, Vol. 27,* S.B. Hooker, E.R. Firestone, and J.G. Acker, Eds., NASA Goddard Space Flight Center, Greenbelt, Maryland, 46 pp.

——, 2000: "Overview of Measurement and Data Analysis Protocols" In: G.S. Fargion and J.L. Mueller, Ocean Optics Protocols for Satellite Ocean Color Sensor Validation, Revision 2. *NASA Tech. Memo. 2000–209966,* NASA Goddard Space Flight Center, Greenbelt, Maryland, 87–97.

——, 2002: "Overview of Measurement and Data Analysis Protocols." In: J.L. Mueller and G.S. Fargion, Ocean Optics Protocols for Satellite Ocean Color Sensor Validation, Revision 3, Volume 1. *NASA Tech. Memo. 2002–210004/Rev3–Vol1,* NASA Goddard Space Flight Center, Greenbelt, Maryland, 123–137.

——, 2003: "Overview of Measurement and Data Analysis Methods." In: J.L. Mueller and 17 Coauthors, Ocean Optics Protocols for Satellite Ocean Color Sensor Validation, Revision 4, Volume III: Radiometric Measurements and Data Analysis Protocols. *NASA Tech. Memo. 2003–211621/Rev4–Vol.III,* NASA Goddard Space Flight Center, Greenbelt, Maryland, 1–6.

——, and R.W. Austin, 1992: Ocean Optics Protocols for SeaWiFS Validation. *NASA Tech. Memo. 104566, Vol. 5,* S.B. Hooker and E.R. Firestone, Eds., NASA Goddard Space Flight Center, Greenbelt, Maryland, 43 pp.

——, B.C. Johnson, C.L. Cromer, J.W. Cooper, J.T. McLean, S.B. Hooker, and T.L. Westphal, 1994: The Second SeaWiFS Intercalibration Round-Robin Experiment, SIRREX-2, June 1993. *NASA Tech. Memo. 104566, Vol. 16,* S.B. Hooker and E.R. Firestone, Eds., NASA Goddard Space Flight Center, Greenbelt, Maryland, 121 pp.

——, and R.W. Austin, 1995: Ocean Optics Protocols for SeaWiFS Validation, Revision 1. *NASA Tech. Memo. 104566, Vol. 25,* S.B. Hooker, E.R. Firestone, and J.G. Acker, Eds., NASA Goddard Space Flight Center, Greenbelt, Maryland, 66 pp.

——, B.C. Johnson, C.L. Cromer, S.B. Hooker, J.T. McLean, and S.F. Biggar, 1996: The Third SeaWiFS Intercalibration Round-Robin Experiment (SIRREX-3), 19–30 September 1994. *NASA Tech. Memo. 104566, Vol. 34,* S.B. Hooker, E.R. Firestone, and J.G. Acker, Eds., NASA Goddard Space Flight Center, Greenbelt, Maryland, 78 pp.

——, and A. Morel, 2003: "Fundamental Definitions, Relationships and Conventions." In: J.L. Mueller and 4 Coauthors, Ocean Optics Protocols for Satellite Ocean Color Sensor Validation, Revision 4, Volume I: Radiometric Measurements and Data Analysis Protocols. *NASA Tech. Memo. 2003–211621/Rev4–Vol.I,* NASA Goddard Space Flight Center, Greenbelt, Maryland, 11–30.

O'Reilly, J.E., S. Maritorena, B.G. Mitchell, D.A. Siegel, K.L. Carder, S.A. Garver, M. Kahru, and C. McClain, 1998: Ocean color chlorophyll algorithms for SeaWiFS. *J. Geophys. Res.,* **103,** 24,937–24,953.

——, and 24 Coauthors, 2000: SeaWiFS Postlaunch Calibration and Validation Analyses, Part 3. *NASA Tech. Memo. 2000–206892, Vol. 11,* S.B. Hooker and E.R. Firestone, Eds., NASA Goddard Space Flight Center, 49 pp. 1,907–1,925.

Riley, T., and S. Bailey, 1998: The Sixth SeaWiFS/SIMBIOS Intercalibration Round-Robin Experiment (SIRREX-6) August–December 1997. *NASA Tech. Memo. 1998–206878,* NASA Goddard Space Flight Center, Greenbelt, Maryland, 26 pp.

Siegel, D.A., M.C. O'Brien, J.C. Sorensen, D. Konnoff, E.A. Brody, J.L. Mueller, C.O. Davis, W.J. Rhea, and S.B. Hooker, 1995: Results of the SeaWiFS Data Analysis Round-Robin (DARR), July 1994. *NASA Tech. Memo. 104566, Vol. 26,* S.B. Hooker and E.R. Firestone, Eds., NASA Goddard Space Flight Center, Greenbelt, Maryland, 58 pp.

Smith, R.C., and K.S. Baker, 1984: The analysis of ocean optical data. *Ocean Optics VII,* M. Blizard, Ed., *SPIE,* **478,** 119–126.

Toole, D.A., D.A. Siegel, D.W. Menzies, M.J. Neumann, and R.C. Smith, 2000: Remote sensing reflectance determinations in the coastal ocean environment—impact of instrumental characteristics and environmental variability. *Appl. Opt.,* **39,** 456–469.

Zibordi, G., J.P. Doyle, and S.B. Hooker, 1999: Offshore tower shading effects on in-water optical measurements. *J. Atmos. Oceanic Tech.,* **16,** 1,767–1,779.

——, D. D'Alimonte, D. van der Linde, J-F. Berthon, S.B. Hooker, J.L. Mueller, G. Lazin, and S. McLean, 2002: The Eighth SeaWiFS Intercalibration Round-Robin Experiment (SIRREX-8), September–December 2001. *NASA Tech. Memo. 2002–206892, Vol. 20,* S.B. Hooker and E.R. Firestone, Eds., NASA Goddard Space Flight Center, Greenbelt, Maryland, 39 pp.

——, F. Mélin, S.B. Hooker, D. D'Alimonte, and B. Holben, 2004: An autonomous above-water system for the validation of ocean color radiance data. *Trans. IEEE Trans. Geosci. Remote Sensing.,* **42,** 401–415.

——, B. Holben, S.B. Hooker, F. Mélin, J-F. Berthon, I. Slutsker, D. Giles, D. Vandemark, H. Feng, K. Rutledge, G. Schuster, and A. Al Mandoos, 2006: A Network for Standardized Ocean Color Validation Measurements. *Eos, Trans. Amer. Geophys. Union*, **84,** 293, 297.